

# Chemical modification of nitrocellulose by grafting sodium carboxymethyl

Shiyong Li (✉ [lisy0613@njust.edu.cn](mailto:lisy0613@njust.edu.cn))

Nanjing University of Science and Technology School of Chemical Engineering <https://orcid.org/0000-0002-5598-2238>

Yu Li

Nanjing University of Science and Technology

Yajun Ding

Nanjing University of Science and Technology

Ye Yuan

Luzhou North chemical industries

Zhongliang Xiao

Nanjing University of Science and Technology

---

## Research Article

**Keywords:** Nitrocellulose, Sodium carboxymethyl-nitrocellulose, Thermal stability, Flame suppression ion

**Posted Date:** June 23rd, 2022

**DOI:** <https://doi.org/10.21203/rs.3.rs-1672478/v1>

**License:**   This work is licensed under a Creative Commons Attribution 4.0 International License.

[Read Full License](#)

---

# Abstract

Introducing deterrents improves the thermal stability of nitrocellulose of propellant surface, but is accompanied with inevitable problems, such as migration, residue, smoke flame, and so on. In this paper, sodium carboxymethyl function groups were chemically grafted to nitrocellulose molecular chains by reaction of denitration and following etherification, which provide thermal stability, flame suppression ion without migration. Various structure characterizations were conducted and confirmed a sodium carboxymethyl-nitrocellulose (CMNC) was prepared successfully. The number of sodium carboxymethyl groups linked to nitrocellulose chains was affected by both denitration and etherification. The results showed that the thermal stability of CMNC improved with the increase of bearing sodium carboxymethyl groups and was better than that of original NC sample. Meanwhile, the thermal decomposition behaviors and decomposition products of CMNC are similar to that of NC at temperature of the first DTG peak  $T_1$  and that of CMC at temperatures of the second DTG peak  $T_2$ . This work provided a way for designing gun propellant with progressive burning, anti-migration and flame suppression simultaneously.

## 1. Introduction

Nitrocellulose is obtained from esterification between hydrogen groups on cellulose and nitrate groups in an acidic medium. The number of hydroxyl groups replaced by nitrate groups determines the nitrogen content that is usually more than 12.5% when used in military (Alinat et al. 2015; Onwukamike et al. 2019). Nitrocellulose is an irreplaceable binder for gun propellant for small to medium caliber weapon. In practical application, improved thermal stability of nitrocellulose of gun propellant surface is required to reduce the chamber pressure and increase the muzzle velocity of projectile, usually realized by adding deterrents with low molecular weight such as phthalate ester, camphor or dinitrotoluene (Liang et al. 2021; Li et al. 2021; Yang et al. 2020). However, the thermal stability could become worse due to the migration of these deterrents in nitrocellulose, resulting in high firing pressure and the risk of explosion (Steve et al. 2011; Boulkadid et al. 2016). Meanwhile, the low oxygen balance of deterrents results in intense flame during shooting, which not only exposes the position, but also reduces the aiming accuracy (Brožek-Mucha 2017; Aurell et al. 2019). Hence, it is urgent to develop a novel strategy to address both migration and flame of deterred propellant.

In order to solve or alleviate the migration of deterrents in nitrocellulose, polymeric deterrents were developed as alternative (Manning et al. 2017). However, the migration of polymeric deterrent could not be inhibited completely. Our team also made some attempts on the anti-migration of deterrents. Li et al. (Li et al. 2020b; Li et al. 2021) conducted denitration strategy to improve the thermal stability of nitrocellulose at the molecular level, which solved the migration problem by reducing the nitrogen content of nitrocellulose on the surface of propellant without introduction of any deterrents.

However, the denitration strategy can also reduce the oxygen balance of nitrocellulose matrix and cause intense flame during shooting by reducing part of nitrate groups in nitrocellulose. It is an effective means to inhibit the flame by adding inorganic alkali metal salts such as sodium salt or potassium salt (Jiang et

al. 2019; Sridhar Iya et al. 1975; Birchall 1970). The inorganic alkali metal salts decompose into M· radicals during burning and react with H· and OH· radicals in gas, terminating the chain reaction of flame generation (Hindiyarti et al. 2006; Babushok et al. 2017; Shen et al. 1991; Omar et al. 2022). However, inorganic alkali metal salts are difficult to decompose and easy to convert into smoke in the burning process. Previous reports presented that organometal salts could effectively relieve the smoke problem of inorganic alkali metal salts due to their low decomposition temperature (Bracuti et al. 1983).

Inspired by the flame retardancy of cellulose modified by carboxymethyl metal salt (Guo et al. 2021; Hu et al. 2019), a strategy of combining denitration and etherification of nitrocellulose was proposed. Specifically, nitrocellulose was denitrated by reacting with hydrazine hydrate to transform part of nitrate groups into hydroxyl groups, followed with carboxymethylation that these hydroxy groups were esterized in the presence of chloroacetic acid, leading to sodium carboxymethyl-nitrocellulose (CMNC) finally. The effect of the preparation process on the structure and thermal properties of CMNC were studied. As expected, CMNC with chemically grafted sodium carboxymethyl groups exhibited improved thermal stability of nitrocellulose without adding deterrents. Meanwhile, CMNC could be considered as an organic sodium salt, which eliminated the flame without increasing smoke concentration. This paper not only presented an effective way of preparing CMNC, but also provided a foundation of designing a gun propellant with anti-migration, progressive burning and flame suppression.

## 2. Materials And Methods

### 2.1. Materials

Nitrocellulose (nitrogen content: 13.15 wt.%) was obtained from Luzhou North Chemical Industries Co., Ltd. Sodium carboxymethyl cellulose (average MW: 250000, DS: 0.9) was purchased from Acros Organics Co., Ltd. Sodium hydroxide (99.5 wt.%) was obtained from Sigma Aldrich Co., Ltd. Chloroacetic acid (99 wt.%) was purchased from Shanghai Bailingwei Chemical Technology Co., Ltd. Anhydrous ethanol (95 vol%), hydrazine hydrate (85 wt.%) and hydrochloric acid (36 wt.%) were obtained from Sinopharm Chemical Reagent Co., Ltd. All the above reagents were analytical purity (AR) and used as received without further purification. Deionized water was used throughout the experiments.

### 2.2. Methods

Sodium carboxymethyl-nitrocellulose (CMNC) was prepared by removing the nitrate groups in nitrocellulose and subsequently introducing sodium carboxymethyl ( $-\text{CH}_2\text{COONa}$ ) functional groups through etherification reaction. The CMNC preparation process is illustrated in Scheme 1.

#### 2.2.1. Preparation of low nitrogen nitrocellulose (LNNC)

Initially, the NC was dried in a 60 °C water bath oven for 12 h. Anhydrous ethanol and 85 wt.% hydrazine hydrate were used to prepare hydrazine hydrate ethanol solutions with different mass fractions. The hydrazine hydrate solutions were prepared with 3 wt.%, 9 wt.% and 15 wt.% for comparative study. 3 g

dried NC was added into a three-necked flask containing 40 mL of hydrazine hydrate ethanol solution. The denitration reaction of NC was conducted at a constant temperature of 65 °C for 2 h with magnetic stirring. Subsequently, the mixture was transferred to an ice bath to stop the reaction quickly. Then, the modified NC was washed with deionized water and anhydrous ethanol in turn for 3 times, followed by drying in a water bath oven at 65 °C for 24 h. After that, LNNC sample was obtained.

## 2.2.2. Preparation of sodium carboxymethyl-nitrocellulose (CMNC)

Typically, take the molar ratio of 6.1:2.4:1 (sodium hydroxide/chloroacetic acid/NC) as an example, the LNNC sample (before drying) and 10 mL NaOH aqueous solution with 1.5 wt.% were added to a 100 mL three-necked flask. LNNC was alkalinized at 35 °C in water bath for 1 h with continuous magnetic stirring. Then, the water bath temperature was raised to 48 °C and a solution prepared previously with 25 mL 3.96 wt.% NaOH anhydrous ethanol solution, 1.637 g chloroacetic acid and 10 mL anhydrous ethanol was added to start etherification reaction. The water bath heating program during etherification was divided into three stages: 48 °C for 30 min, 63 °C for 45 min, and 73 °C for 15 min. After the reaction, the three-necked flask was transferred to an ice bath quickly. The mixture was then transferred to a beaker containing 100 mL 2.72 wt.% hydrochloric acid anhydrous ethanol solution and stirred magnetically for 20 min to neutralize the excess NaOH. After that, the products were washed with ethanol several times. Finally, sodium carboxymethyl-nitrocellulose (CMNC) samples were obtained by drying the product in a 60 °C water bath oven for 12 h. The number of introducing sodium carboxymethyl (-CH<sub>2</sub>COONa) functional groups can be easily and effectively regulated by changing the molar ratio of sodium hydroxide/chloroacetic acid/NC. A series of CMNC samples were prepared. The labels and experimental parameters of samples were listed in Table 1. The chemical mechanism of CMNC preparation was summarized as the follows:

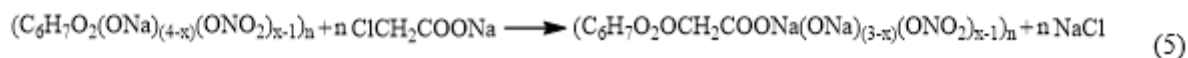
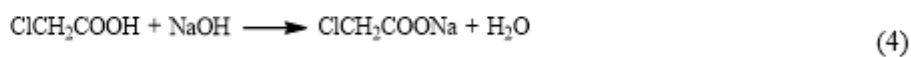
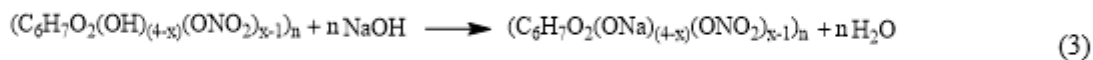
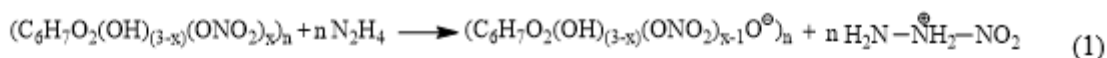


Table 1  
The labels and experimental parameters of samples.

Samples	Denitration conditions	Etherification conditions		
	Concentration of hydrazine hydrate solution/wt.%	The molar ratio of sodium hydroxide/chloroacetic acid/NC	Reagent volume/mL	Reaction time/h
LNNC	9	-	-	-
CMNC-1	3	6.1:2.4:1	35	1.5
CMNC-2	9	6.1:2.4:1	35	1.5
CMNC-3	15	6.1:2.4:1	35	1.5
CMNC-4	9	4:2.4:1	35	1.5
CMNC-5	9	3:2.4:1	35	1.5

## 2.3. Characterization

### 2.3.1. Structural characterization and elemental analysis

The functional groups of the samples were characterized by Fourier transform infrared spectrometer (FTIR, Thermo Fisher Nicolet iS20, America). The spectral resolution was  $4\text{ cm}^{-1}$  and the range of measurement was  $4000 - 700\text{ cm}^{-1}$ . Scanning electron microscope equipped with energy-dispersive X-ray spectroscopy (SEM, FEI Quanta 250 FEG, America) with 5 KV accelerating voltage was used to characterize the microstructure and elemental mapping image of the samples. Surface elemental analysis of the samples were performed by an X-ray photoelectron spectrometer (XPS, Thermo Scientific ESCALAB 250Xi, America) probed with a monochromatic Al K $\alpha$  radiation source ( $h\nu = 1486.65\text{ eV}$ ) in a vacuum chamber. The binding energies of the spectra were calibrated according to the C 1s peak at 284.6 eV. The nitrogen (N) elemental analysis was undertaken with an Elemental Analyzer (EA, Elementar UNICUBE, Germany). The Sodium (Na) content was evaluated by ICP-OES (Agilent 7700, America).

### 2.3.2. Thermal analysis

The thermal decomposition properties were investigated by thermogravimetric analysis (TG, Mettler Toledo SDTA 851E Instruments, America). TG experiments were carried out under Ar atmosphere ( $20\text{ mL}\cdot\text{min}^{-1}$ ) at a heating rate of  $10\text{ }^{\circ}\text{C}\cdot\text{min}^{-1}$  from 50 to 700  $^{\circ}\text{C}$ . TG-FTIR measurements were carried out using a TG analyzer (TG, Netzsch STA 449F5, Germany) coupled with a FTIR spectrometer (Bruker VERTE X80, Germany), providing a continuous detection of the gaseous products in the thermal decomposition process. The experiments were performed in Ar at a purge rate of  $20\text{ mL}\cdot\text{min}^{-1}$  and heated at  $10\text{ }^{\circ}\text{C}\cdot\text{min}^{-1}$  from 50 to 700  $^{\circ}\text{C}$ . The scanning range of the FTIR spectra varied between  $4500$  and  $650\text{ cm}^{-1}$  at a resolution of  $4\text{ cm}^{-1}$  with 8 scans per sampling.

### 3. Results And Discussions

#### 3.1. Structural characterization and elemental analysis

The FTIR spectra of CMNC, NC, and commercial CMC samples were shown in Fig. 1(a) and the absorption bands of functional groups were summarized as shown in Table 2. All spectra were normalized in light of that for all samples, the peak intensity at around  $1160\text{ cm}^{-1}$  attributed to the asymmetric vibration of the C - O-C in  $\beta$ -glycosidic linkage was believed to be unchanged, which was convenient for comparing the change of characteristic peaks of samples obtained from different experiment conditions. From Fig. 1(a), there are different offsets near  $1730 - 1490\text{ cm}^{-1}$  for five CMNC samples. Those characteristic peaks of different samples were fitted and deconvoluted into two peaks:  $\approx 1639\text{ cm}^{-1}$  ( $-\text{ONO}_2$ ) and  $1587\text{ cm}^{-1}$  ( $\text{COO}^-$  or  $\text{COONa}$  in  $-\text{OCH}_2\text{COONa}$ ), as shown in Fig. 1(b) and 1(c). From Fig. 1(b), with the increase of the degree of denitration, the number of  $-\text{OCH}_2\text{COONa}$  introduced to LNNC samples increases under the same subsequent etherification reaction conditions. As seen in Fig. 1(c), the degree of etherification gradually decreases with the decrease of the degree of denitration. Under the same degree of etherification, the nitrocellulose molecular chain with high denitration degree is more likely to react with carboxymethyl groups. This may be because the sequence of  $-\text{ONO}_2$  removed from the glucose units in nitrocellulose molecule is  $\text{C3} > \text{C6} > \text{C2}$ , while in the process of etherification, the order of  $-\text{OCH}_2\text{COONa}$  introduced into glucose ring is  $\text{C2} \approx \text{C6} > \text{C3}$  (Shukla and Hill 2012; Shui et al. 2017). From the spectra of the samples in Fig. 1, the CMNC sample presents both characteristic peaks of  $-\text{ONO}_2$  and peaks of introduced  $-\text{OCH}_2\text{COONa}$ , which proves the CMNC has been successfully prepared.

Table 2

Identification of prevalent bands in FTIR spectra of samples (Casaburi et al. 2018; Golbaghi et al. 2017; Zhao et al. 2016; You et al. 2016; Luo et al. 2019a; Kumar et al. 2018; Wongvitvichot et al. 2021; Wang et al. 2018; Mu et al. 2016; Wang et al. 2021).

No.	Absorption range/ $\text{cm}^{-1}$	Characteristic groups
1	3375	$-\text{OH}$ stretching vibration
2	2900	$-\text{CH}_2-$ stretching vibration
3	1160	Asymmetric oxygen bridge stretching vibration
4	1587	$\text{COO}^-$ or $\text{COONa}$ stretching vibration
5	821	$-\text{ONO}_2$ stretching vibration
6	1273	$-\text{ONO}_2$ symmetric stretching
7	1639	$-\text{ONO}_2$ asymmetric stretching vibration

XPS experiments were employed to support the FTIR data and to further understand the chemical property and chemical bonding of the surface region of CMNC samples and their precursors. The full surface survey and individual spectra of samples were shown in Fig. 2(a). The total intensity for each sample has been normalized to unity. It can be seen that the characteristic peaks of NC, LNNC, commercial CMC and CMNC samples are C 1s, O 1s, N 1s, Na 1s, O Auger and Na Auger (Yu et al. 2013; Wang et al. 2017). Meanwhile, under the same degree of etherification, with the increasing degree of denitration, the characteristic peak intensity of Na element gradually increases and the characteristic peak of N element gradually disappears. Under the same degree of denitration, with the increasing degree of etherification, the characteristic peaks of Na element are gradually enhanced. The curve fitting with a high resolution of C 1s and O 1s spectra revealed the functional compositions were carbon and oxygen species for samples, as shown in Fig. 2(b) and (c). The C 1s peak of the CMNC (1, 2 and 3) samples were fitted to five Gaussian curves. Among them, the Gaussian peak at 283.1 eV is belonged to C - C and C - H; the Gaussian peak at 284.4 eV is assigned to the characteristic peak of C - O; the characteristic peak at 285.3 eV corresponding to the characteristic peak of C = O or O - C=O was observed (Mansur et al. 2017; Li et al. 2020a; Cui et al. 2020). The characteristic peak at 286.3 eV is correspond to the characteristic peak of C-ONO<sub>2</sub> (Lu et al. 2021); the characteristic peak at 286.6 eV is attributed to the characteristic peak of O = C - O<sup>-</sup> (Samadder et al. 2020; Liu et al. 2017). Under the same etherification conditions, the characteristic peak of C - ONO<sub>2</sub> gradually weakened and the characteristic peak of O = C - O<sup>-</sup> gradually elevated with the increasing denitration degree. For Fig. 3(c), the O 1s peak of the CMNC sample is fitted to four Gaussian peaks. Among them, the characteristic peak at 529.3 eV is assigned to the O = C characteristic peak; the characteristic peak at 530.5 eV is belonged to the characteristic peak of O - C (Hu et al. 2018; Bai et al. 2020; Yuan et al. 2021); the characteristic peak at 531.3 eV is correspond to the characteristic peak of C - OO<sup>-</sup> (Mansur et al. 2017; He et al. 2020); the peak at 532.2 eV is attributed to the characteristic peak of O - NO<sub>2</sub> (Luo et al. 2019b). Under the same etherification conditions of CMNC (2, 4 and 5) samples, with the increase of denitration degree, the characteristic peak of C - OO<sup>-</sup> gradually increased and the characteristic peak of O - NO<sub>2</sub> gradually weakened. The above results are consistent with the FTIR results, which confirms the -OCH<sub>2</sub>COONa groups have been introduced in nitrocellulose chemically and the CMNC samples have been prepared successfully.

The morphologies of the original NC and CMNC-3 samples were observed by SEM, as shown in Fig. 3(a) and 3(b), respectively. From the SEM images, the CMNC sample exhibits a fiber structure similar to NC and a rougher surface. Meanwhile, the local element content analysis for CMNC was performed and presented in Fig. 3(b), indicating the content of Na was 6.23 wt.%. Furthermore, uniform distribution of C, O, N and Na elements were demonstrated by the corresponding element mapping (Fig. 3c-f), indicating that the CMNC sample was prepared successfully.

The elemental analyses of NC, LNNC, CMC and CMNC samples were displayed in Fig. 4. The nitrogen content of NC and LNNC was 12.152 wt.% and 6.225 wt.%, respectively. The CMC samples do not contain nitrogen. For CMNC (1, 2 and 3) samples, the nitrogen content of the samples decreased gradually with the increase of denitration degree. With the same degree of denitration, the nitrogen content of the

samples of CMNC (2, 4 and 5) gradually increased with the decrease of the degree of etherification, which could be caused by the introduction of  $-\text{OCH}_2\text{COONa}$  into the NC molecular chains. Another reason for this result is that sodium hydroxide was used to provide an alkaline environment during the etherification reaction, which has a certain alkaline hydrolysis effect on NC as a strong base (Lee et al. 2019). Both NC and LNNC samples contained a small amount of Na, which may be attributed to the alkalizing step during nitrocellulose production (Urbanski et al. 1965). For CMNC (1, 2 and 3) samples, with the increase of denitration degree, the sodium content of CMNC samples increased gradually. In the CMNC (2, 4 and 5) samples, under the same denitration conditions, the Na element content gradually decreased with the decreasing degree of etherification. The results of the elemental analysis were consistent with that of FTIR and XPS, which proved forcefully that the structure construction of CMNC could be controlled precisely. Hopefully, the introduction of sodium-containing functional groups ( $-\text{OCH}_2\text{COONa}$ ) will provide a significant flame suppressant effect on CMNC samples.

## 3.2. Thermal decomposition behavior

The curves of thermogravimetric (TG) and its differential (DTG) during thermal decomposition at the heating rate of  $10\text{ }^\circ\text{C}\cdot\text{min}^{-1}$  were shown in Fig. 5.  $T_{\text{in}}$  and  $T_{\text{f}}$  were the initial and ending temperature of main weight loss zone, respectively. The decomposition process of samples can be divided into three stages (Wu et al. 2016). The initial stage was from the beginning of heating to  $T_{\text{in}}$ , during which a slight weight loss phase and the glass transition occurred and the sample dehydrated. The yield of volatiles was extremely low at this stage (Zhang et al. 2019). The second stage started from  $T_{\text{in}}$  to  $T_{\text{f}}$ , featuring main weight loss because the thermal reaction became intensive and a large amount of volatiles were produced (Tudorachi et al. 2012). When the temperature reached  $T_1/T_{\text{max}}$  (temperature of the first DTG peak), the weight loss rate achieved the peak value. Then the DTG curve started to decrease with increasing temperature until the thermogravimetric process ended at  $T_{\text{f}}$ . The third stage was carbonization stage where the TG and DTG curves were almost flat and the residues from the second stage were carbonized (Xu et al. 2020).

The thermal characteristic parameters were presented in Table 3. The  $T_{\text{in}}$ ,  $T_{\text{max}}$  and  $M_{\text{f}}$  (the weight fraction of final residue) values of the CMNC sample are higher than those of the original NC sample. Combing the thermal characteristic parameters and the results of FTIR and XPS of different CMNC samples, a clear trend can be concluded that the more  $-\text{OCH}_2\text{COONa}$  was introduced into the NC molecular chain, the better thermal stability of CMNC was obtained (Guo et al. 2021). Remarkably, CMNC sample exhibited two maximum decomposition rate peaks from the DTG curves. The first at near  $210\text{ }^\circ\text{C}$  is close to the maximum decomposition temperature of NC. The other is near  $290\text{ }^\circ\text{C}$ , which is close to the maximum pyrolysis temperature of CMC (Wu et al. 2016). This indicated that CMNC presented similar thermal decomposition characteristics to both NC and CMC.

Table 3

Thermal behavior parameters of NC, CMC and CMNC samples with  $\beta = 10 \text{ }^\circ\text{C}\cdot\text{min}^{-1}$ .

Parameters	NC	CMNC-1	CMNC-2	CMNC-3	CMNC-5
$T_{in}$ ( $^\circ\text{C}$ )	179.5	155.8	175.8	188.8	166
$T_1/T_{max}$ ( $^\circ\text{C}$ )	205.6	206.3	222.5	225	214
$T_2$ ( $^\circ\text{C}$ )	-	296.8	292.5	280	261.3
$T_f$	245.8	325.2	320.2	326.7	385.17
$M_r$ (%)	15.70	29.74	51.61	61.40	17.46
$T_{in}$ : initial devolatilization temperature; $T_1/T_{max}$ : temperature of the first DTG peak; $T_2$ : temperatures of the second DTG peak; $T_f$ : temperature at the end of the DTG peak; $M_r$ : weight fraction of the final residue.					

The TG-FTIR simultaneous analysis technique was employed to investigate the thermal degradation process of NC and CMNC-2 sample with real-time detection at a heating rate of  $10 \text{ }^\circ\text{C}\cdot\text{min}^{-1}$ . There is apparent variation in the IR characteristic absorption peaks of the gaseous decomposition products of samples during thermal decomposition process at typical temperatures, including the temperature before decomposition ( $T_x$ , select  $125 \text{ }^\circ\text{C}$  as  $T_x$  temperature),  $T_{in}$ ,  $T_1/T_{max}$ ,  $T_2$ , and  $T_f$ , as shown in Table 3 and Fig. 6(a, b). Most gases produced during sample pyrolysis could be identified through their FTIR peaks (Table 4).

Table 4  
Reported FTIR characteristic peaks from gases generated during thermal degradation (Tudorachi et al. 2012; Chai et al. 2020; Zhao et al. 2021).

No.	Products	Wavenumbers of IR absorption peaks /cm <sup>-1</sup>
1	H <sub>2</sub> O	3600–4000 cm <sup>-1</sup>
2	CO <sub>2</sub>	2300–2380, 660–670 cm <sup>-1</sup>
3	HCHO	2700–2900 cm <sup>-1</sup> , 1720–1740 cm <sup>-1</sup>
4	N <sub>2</sub> O	2200–2300 cm <sup>-1</sup>
5	CO	2109–2194 cm <sup>-1</sup>
6	NO	1760–1965 cm <sup>-1</sup>
7	NO <sub>2</sub>	1593–1639 cm <sup>-1</sup>
8	HCOOH	1080–1128 cm <sup>-1</sup>
9	C = O	1769 cm <sup>-1</sup>
10	-OH	1187 cm <sup>-1</sup> , 3200–3400 cm <sup>-1</sup>

Figure 6(a) showed the real-time FTIR spectrum of NC sample. The FTIR absorption peaks of H<sub>2</sub>O, CO<sub>2</sub> were detected at  $T_x$  and  $T_{in}$ . The initial characteristic gas-phase CO<sub>2</sub> peak at 2360 cm<sup>-1</sup> was attributed to the air flow fluctuation found within the air vent inside the FTIR beam chamber (due to the presence of CO in the laboratory atmosphere). Additionally, in this temperature range, the structure of nitrocellulose was relatively stable and there was no thermal damage. When the temperature increased to  $T_1/T_{max}$ , the gaseous products such as H<sub>2</sub>O, HCHO, CO<sub>2</sub>, N<sub>2</sub>O, CO, NO, NO<sub>2</sub> and HCOOH were detected. The peak at 1769 cm<sup>-1</sup> was attributed to the C = O stretching bands of HCHO, generated from the -CH<sub>2</sub>ONO<sub>2</sub> group. Evolution of the HCOOH gas was due to the secondary autocatalytic reactions of NC. At the end of the decomposition process ( $T_f$ ), the FTIR absorption peaks of H<sub>2</sub>O, CO<sub>2</sub>, NO and HCOOH were still easily identifiable in Fig. 6(a) (Chai et al. 2020; Zhao et al. 2021). Figure 6(b) presented the FTIR spectra of CMNC-2 at typical temperatures in the thermal decomposition. At the temperature of  $T_x$  and  $T_{in}$ , the peaks of H<sub>2</sub>O and CO<sub>2</sub> were assigned to the same event with the previous discussion. At the temperature of  $T_1/T_{max}$  and  $T_2$ , the main evolved gases were H<sub>2</sub>O, CO<sub>2</sub>, N<sub>2</sub>O, NO<sub>2</sub>, and HCOOH. The generation of nitrogen oxides were attributed to the decomposition of -ONO<sub>2</sub> on the molecular chain during heating. This is similar to the thermal decomposition characteristics of NC (Zhao et al. 2021). At  $T_2$ , the absorption bands in the FTIR spectrum were corresponding to H<sub>2</sub>O, CO<sub>2</sub>, HCHO, and CO. In addition, a band with reduced intensity at 1187 cm<sup>-1</sup> and a wide absorption band between 3200–3400 cm<sup>-1</sup>, corresponding to

$\nu$ OH vibrations, can be attributed to ethanol fragments. The decomposition products at this temperature are similar to the decomposition process of CMC (Tudorachi et al. 2012). At  $T_f$ ,  $H_2O$  and  $CO_2$  were observed, which might be due to the residual organic matrix. According to the real-time detection of gas generation by TG-FTIR during thermal decomposition, CMNC exhibited a similar thermal decomposition behaviors with NC and CMC to some extent and a better thermal stability than NC, leading to potential applications in propellant with certain flame retardant properties through chemical modification. Otherwise, the chemical grafting of sodium carboxymethyl groups through partly denitration and etherification provides an inspiration of designing a new type of cellulose derivative with burn progressive, flame suppression and anti-migration properties simultaneously. It is expected to become a new type of cellulose derivative with energy containing and anti-migration properties.

## 4. Conclusions

According to the chemical modification method, we used hydrazine hydrate as a denitration reagent to remove part of the nitrate groups on nitrocellulose with high nitrogen content and converted functional groups into hydroxyl groups. Then sodium hydroxide and chloroacetic acid were employed as etherification reagents to introduce the sodium carboxymethyl functional groups into the molecular chains of nitrocellulose to prepare sodium carboxymethyl-nitrocellulose (CMNC) successfully. The results were shown as follows:

(1) For the first time, the design strategy of denitration and then etherification was adopted, and CMNC was prepared successfully. Structural characterization and elemental analysis of the as-prepared CMNC samples were performed by FTIR, XPS, SEM, EA and ICP-OES. The results showed that the denitration reaction in the first step transformed part of the nitrate groups ( $-ONO_2$ ) in nitrocellulose into hydroxyl groups ( $-OH$ ), and the etherification reaction in the second step introduced the sodium carboxymethyl groups ( $-OCH_2COONa$ ) into the nitrocellulose successfully. All results confirmed that CMNC was prepared successfully.

(2) The thermal decomposition behavior and thermal decomposition products of NC, CMC and CMNC samples were compared by TG-FTIR. The results of TG showed that CMNC exhibited a higher thermal stability than original NC and a similar the thermal decomposition behavior of to NC and CMC to some extent. CMNC was expected to be a new energetic polymer deterrent with anti-migration properties.

## References

1. Alinat E, Delaunay N, Archer X, Mallet J-M, Gareil P (2015) A new method for the determination of the nitrogen content of nitrocellulose based on the molar ratio of nitrite-to-nitrate ions released after alkaline hydrolysis. *J Hazard Mater* 286:92–99. doi:<https://doi.org/10.1016/j.jhazmat.2014.12.032>
2. Aurell J, Holder AL, Gullett BK, McNesby K, Weinstein JP (2019) Characterization of M4 carbine rifle emissions with three ammunition types. *Environ Pollut* 254:112982–112991. doi:<https://doi.org/10.1016/j.envpol.2019.112982>

3. Babushok VI, Linteris GT, Hoorelbeke P, Roosendans D, van Wingerden K (2017) Flame inhibition by potassium-containing compounds. *Combust Sci Technol* 189:2039–2055.  
doi:<https://doi.org/10.1080/00102202.2017.1347162>
4. Bai C, Wang L, Zhu Z (2020) Adsorption of Cr(III) and Pb(II) by graphene oxide/alginate hydrogel membrane: Characterization, adsorption kinetics, isotherm and thermodynamics studies. *Int J Biol Macromol* 147:898–910. doi:<https://doi.org/10.1016/j.ijbiomac.2019.09.249>
5. Birchall JD (1970) On the mechanism of flame inhibition by alkali metal salts. *Combust Flame* 14:85–95. doi:[https://doi.org/10.1016/S0010-2180\(70\)80013-X](https://doi.org/10.1016/S0010-2180(70)80013-X)
6. Boulkadid MK, Lefebvre MH, Jeunieu L, Dejeaifve A (2016) Temperature sensitivity of propellant combustion and temperature coefficients of gun performance. *Cent Eur J Energ Mat* 13:1005–1022
7. Bracuti A, Bottei L, Davis R (1983) Potential multipurpose additives: flash-erosion suppressant. Army Armament Research and Development Center Dover NJ Large Caliber Weapon Systems Lab, Dover, New Jersey
8. Brožek-Mucha Z (2017) A study of gunshot residue distribution for close-range shots with a silenced gun using optical and scanning electron microscopy, X-ray microanalysis and infrared spectroscopy. *Sci Justice* 57:87–94. doi:<https://doi.org/10.1016/j.scijus.2016.11.004>
9. Casaburi A, Montoya Rojo Ú, Cerrutti P, Vázquez A, Foresti ML (2018) Carboxymethyl cellulose with tailored degree of substitution obtained from bacterial cellulose. *Food Hydrocolloid* 75:147–156. doi:<https://doi.org/10.1016/j.foodhyd.2017.09.002>
10. Chai H, Duan Q, Cao H, Li M, Sun J (2020) Effects of nitrogen content on pyrolysis behavior of nitrocellulose. *Fuel* 264:116853. doi:<https://doi.org/10.1016/j.fuel.2019.116853>
11. Cui X, Honda T, Asoh T-A, Uyama H (2020) Cellulose modified by citric acid reinforced polypropylene resin as fillers. *Carbohydr Polym* 230:115662–115668.  
doi:<https://doi.org/10.1016/j.carbpol.2019.115662>
12. Golbaghi L, Khamforoush M, Hatami T (2017) Carboxymethyl cellulose production from sugarcane bagasse with steam explosion pulping: Experimental, modeling, and optimization. *Carbohydr Polym* 174:780–788. doi:<https://doi.org/10.1016/j.carbpol.2017.06.123>
13. Guo X, Wang Y, Ren Y, Liu X (2021) Fabrication of flame retardant lyocell fibers based on carboxymethylation and aluminum ion chelation. *Cellulose* 28:6679–6698.  
doi:<https://doi.org/10.1007/s10570-021-03931-6>
14. He H, Cheng M, Liang Y, Zhu H, Sun Y, Dong D, Wang S (2020) Intelligent cellulose nanofibers with excellent biocompatibility enable sustained antibacterial and drug release via a pH-responsive mechanism. *J Agr Food Chem* 68:3518–3527. doi:<https://doi.org/10.1021/acs.jafc.9b06588>
15. Hindiyarti L, Frandsen F, Livbjerg H, Glarborg P (2006) Influence of potassium chloride on moist CO oxidation under reducing conditions: Experimental and kinetic modeling study. *Fuel* 85:978–988. doi:<https://doi.org/10.1016/j.fuel.2005.10.021>
16. Hu W, Lu L, Li Z, Shao L (2019) A facile slow-gel method for bulk Al-doped carboxymethyl cellulose aerogels with excellent flame retardancy. *Carbohydr Polym* 207:352–361.

doi:<https://doi.org/10.1016/j.carbpol.2018.11.089>

17. Hu Z, Wang Y, Omer AM, Ouyang X (2018) Fabrication of ofloxacin imprinted polymer on the surface of magnetic carboxylated cellulose nanocrystals for highly selective adsorption of fluoroquinolones from water. *Int J Biol Macromol* 107:453–462. doi:<https://doi.org/10.1016/j.ijbiomac.2017.09.009>
18. Jiang H, Bi M, Li B, Ma D, Gao W (2019) Flame inhibition of aluminum dust explosion by  $\text{NaHCO}_3$  and  $\text{NH}_4\text{H}_2\text{PO}_4$ . *Combust Flame* 200:97–114. doi:<https://doi.org/10.1016/j.combustflame.2018.11.016>
19. Kumar A, Rao KM, Han SS (2018) Mechanically viscoelastic nanoreinforced hybrid hydrogels composed of polyacrylamide, sodium carboxymethylcellulose, graphene oxide, and cellulose nanocrystals. *Carbohydr Polym* 193:228–238. doi:<https://doi.org/10.1016/j.carbpol.2018.04.004>
20. Lee Y, Lee J, Choe W, Kim T, Lee J-Y, Kho Y, Choi K, Zoh K-D (2019) Distribution of phthalate esters in air, water, sediments, and fish in the Asan Lake of Korea. *Environ Int* 126:635–643. doi:<https://doi.org/10.1016/j.envint.2019.02.059>
21. Li C, Ma H, Venkateswaran S, Hsiao BS (2020a) Highly efficient and sustainable carboxylated cellulose filters for removal of cationic dyes/heavy metals ions. *Chem Eng J* 389:123458–123470. doi:<https://doi.org/10.1016/j.cej.2019.123458>
22. Li S, Li Y, Ding Y, Liang H, Xiao ZL (2021) One-step green method to prepare progressive burning gun propellant through gradient denitration strategy. *Def Technol*. doi:<https://doi.org/10.1016/j.dt.2021.11.009>
23. Li S, Tao Z, Ding Y, Liang H, Zhao X, Xiao Z, Li C, Ou J (2020b) Gradient denitration strategy eliminates phthalates associated potential hazards during gun propellant production and application. *Propellants Explos Pyrotech* 45:1156–1167. doi:<https://doi.org/10.1002/prop.202000006>
24. Liang H, Ding Y, Li S, Xiao Z (2021) Combustion performance of spherical propellants deterred by energetic composite deterring agents. *ACS Omega* 6:13024–13032. doi:<https://doi.org/10.1021/acsomega.1c00637>
25. Liu C, Jin R-N, Ouyang X-k, Wang Y-G (2017) Adsorption behavior of carboxylated cellulose nanocrystal–polyethyleneimine composite for removal of Cr(VI) ions. *Appl Surf Sci* 408:77–87. doi:<https://doi.org/10.1016/j.apsusc.2017.02.265>
26. Lu T, Zhao B, Liu Y, Yan Z, Wang Y, Fu X, Yan Q (2021) Enhanced thermal and energetic properties of NC-based nanocomposites with silane functionalized GO. *Dalton Trans* 50:17766–17773. doi:<https://doi.org/10.1039/D1DT03305K>
27. Luo L, Jin B, Xiao Y, Zhang Q, Chai Z, Huang Q, Chu S, Peng R (2019a) Study on the isothermal decomposition kinetics and mechanism of nitrocellulose. *Polym Test* 75:337–343. doi:<https://doi.org/10.1016/j.polymertesting.2019.02.024>
28. Luo T, Wang Y, Huang H, Shang F, Song X (2019b) An electrospun preparation of the NC/GAP/Nano-LLM-105 nanofiber and its properties. *Nanomaterials* 9:854–868. doi:<https://doi.org/10.3390/nano9060854>

29. Manning T, Wyckoff J, Klingaman K, Panchal V, Rozumov E, Bolognini J, Young MW, Patel S (2017) Enhanced propellant performance via environmentally friendly curable surface coating. *Def Technol* 13:131–142. doi:<https://doi.org/10.1016/j.dt.2017.04.007>
30. Mansur AAP, de Carvalho FG, Mansur RL, Carvalho SM, de Oliveira LC, Mansur HS (2017) Carboxymethylcellulose/ZnCdS fluorescent quantum dot nanoconjugates for cancer cell bioimaging. *Int J Biol Macromol* 96:675–686. doi:<https://doi.org/10.1016/j.ijbiomac.2016.12.078>
31. Mu X, Yu H, Zhang C, Chen X, Cheng Z, Bai R, Wu X, Yu Q, Wu C, Diao Y (2016) Nano-porous nitrocellulose liquid bandage modulates cell and cytokine response and accelerates cutaneous wound healing in a mouse model. *Carbohydr Polym* 136:618–629. doi:<https://doi.org/10.1016/j.carbpol.2015.08.070>
32. Omar D, Jaravel T, Vermorel O (2022) On the controlling parameters of the thermal decomposition of inhibiting particles: A theoretical and numerical study. *Combust Flame* 240:111991. doi:<https://doi.org/10.1016/j.combustflame.2022.111991>
33. Onwukamike KN, Grelier S, Grau E, Cramail H, Meier MAR (2019) Critical review on sustainable homogeneous cellulose modification: why renewability is not enough. *ACS Sustain Chem Eng* 7:1826–1840. doi:<https://doi.org/10.1021/acssuschemeng.8b04990>
34. Samadder R, Akter N, Roy AC, Uddin MM, Hossen MJ, Azam MS (2020) Magnetic nanocomposite based on polyacrylic acid and carboxylated cellulose nanocrystal for the removal of cationic dye. *RSC Adv* 10:11945–11956. doi:<https://doi.org/10.1039/D0RA00604A>
35. Shen S, Leu A, Yeh H (1991) Evaluation method for the effect of salts on the elimination of secondary flames of energetic materials by differential scanning calorimetry. *Thermochim Acta* 177:23–37. doi:[https://doi.org/10.1016/0040-6031\(91\)80082-T](https://doi.org/10.1016/0040-6031(91)80082-T)
36. Shui T, Feng S, Chen G, Li A, Yuan Z, Shui H, Kuboki T, Xu C (2017) Synthesis of sodium carboxymethyl cellulose using bleached crude cellulose fractionated from cornstalk. *Biomass Bioenerg* 105:51–58. doi:<https://doi.org/10.1016/j.biombioe.2017.06.016>
37. Shukla MK, Hill F (2012) Computational elucidation of mechanisms of alkaline hydrolysis of nitrocellulose: dimer and trimer models with comparison to the corresponding monomer. *J Phys Chem A* 116:7746–7755. doi:<https://doi.org/10.1021/jp3042878>
38. Sridhar Iya K, Wollowitz S, Kaskan WE (1975) The mechanism of flame inhibition by sodium salts. *Symposium (International) on Combustion* 15:329–336. doi:[https://doi.org/10.1016/S0082-0784\(75\)80308-0](https://doi.org/10.1016/S0082-0784(75)80308-0)
39. Steve T, Joseph S, Christopher TG, Elisabeth M, Ashley J (2011) Determination of deterrent profiles in nitrocellulose propellant grains using confocal raman microscopy. *Propellants Explos Pyrotech* 36:451–458. doi:<https://doi.org/10.1002/prop.201000081>
40. Tudorachi N, Lipsa R, Mustata FR (2012) Thermal degradation of carboxymethyl starch–g-poly(lactic acid) copolymer by TG–FTIR–MS analysis. *Ind Eng Chem Res* 51:15537–15545. doi:<https://doi.org/10.1021/ie300625c>

41. Urbanski T, Laverton S, Ornaf W (1965) Chemistry and technology of explosives, vol –. vol 1. Pergamon Press, London
42. Wang B, Yang X, Qiao C, Li Y, Li T, Xu C (2018) Effects of chitosan quaternary ammonium salt on the physicochemical properties of sodium carboxymethyl cellulose-based films. *Carbohydr Polym* 184:37–46. doi:<https://doi.org/10.1016/j.carbpol.2017.12.030>
43. Wang N, Jin R, Omer AM, Ouyang X (2017) Adsorption of Pb(II) from fish sauce using carboxylated cellulose nanocrystal: Isotherm, kinetics, and thermodynamic studies. *Int J Biol Macromol* 102:232–240. doi:<https://doi.org/10.1016/j.ijbiomac.2017.03.150>
44. Wang W, Li H, Yang Y, Zhao F, Li H, Xu K (2021) Enhanced thermal decomposition, laser ignition and combustion properties of NC/Al/RDX composite fibers fabricated by electrospinning. *Cellulose* 28:6089–6105. doi:<https://doi.org/10.1007/s10570-021-03957-w>
45. Wongvitvichot W, Pithakratanayothin S, Wongkasemjit S, Chaisuwan T (2021) Fast and practical synthesis of carboxymethyl cellulose from office paper waste by ultrasonic-assisted technique at ambient temperature. *Polym Degrad Stab* 184:109473. doi:<https://doi.org/10.1016/j.polymdegradstab.2020.109473>
46. Wu Z, Wang S, Zhao J, Chen L, Meng H (2016) Thermochemical behavior and char morphology analysis of blended bituminous coal and lignocellulosic biomass model compound co-pyrolysis: Effects of cellulose and carboxymethylcellulose sodium. *Fuel* 171:65–73. doi:<https://doi.org/10.1016/j.fuel.2015.12.057>
47. Xu FX, Zhang X, Zhang F, Jiang LQ, Zhao ZL, Li HB (2020) TG-FTIR for kinetic evaluation and evolved gas analysis of cellulose with different structures. *Fuel* 268:117365–117372. doi:<https://doi.org/10.1016/j.fuel.2020.117365>
48. Yang W, Hu R, Zheng L, Yan G, Yan W (2020) Fabrication and investigation of 3D-printed gun propellants. *Mater Des* 192:108761–108768. doi:<https://doi.org/10.1016/j.matdes.2020.108761>
49. You Y, Zhang H, Liu Y, Lei B (2016) Transparent sunlight conversion film based on carboxymethyl cellulose and carbon dots. *Carbohydr Polym* 151:245–250. doi:<https://doi.org/10.1016/j.carbpol.2016.05.063>
50. Yu X, Tong S, Ge M, Wu L, Zuo J, Cao C, Song W (2013) Adsorption of heavy metal ions from aqueous solution by carboxylated cellulose nanocrystals. *J Environ Sci* 25:933–943. doi:[https://doi.org/10.1016/S1001-0742\(12\)60145-4](https://doi.org/10.1016/S1001-0742(12)60145-4)
51. Yuan J, Yi C, Jiang H, Liu F, Cheng GJ (2021) Direct ink writing of hierarchically porous cellulose/alginate monolithic hydrogel as a highly effective adsorbent for environmental applications. *ACS Appl Polym Mater* 3:699–709. doi:<https://doi.org/10.1021/acsapm.0c01002>
52. Zhang Y, Kang L, Li H, Huang X, Liu X, Guo L, Huang L (2019) Characterization of moxa floss combustion by TG/DSC, TG-FTIR and IR. *Bioresour Technol* 288:121516–121523. doi:<https://doi.org/10.1016/j.biortech.2019.121516>
53. Zhao N, Li J, Gong H, An T, Zhao F, Yang A, Hu R, Ma H (2016) Effects of  $\alpha$ -Fe<sub>2</sub>O<sub>3</sub> nanoparticles on the thermal behavior and non-isothermal decomposition kinetics of nitrocellulose. *J Anal Appl Pyrol*

54. Zhao N, Ma H, Yao E, Yu Z, An T, Zhao F, Yu X (2021) Influence of tailored CuO and Al/CuO nanothermites on the thermocatalytic degradation of nitrocellulose and combustion performance of AP/HTPB composite propellant. Cellulose 28:8671–8691. doi:https://doi.org/10.1007/s10570-021-04060-w

## Scheme

Scheme 1 is available in Supplementary Files section.

## Figures

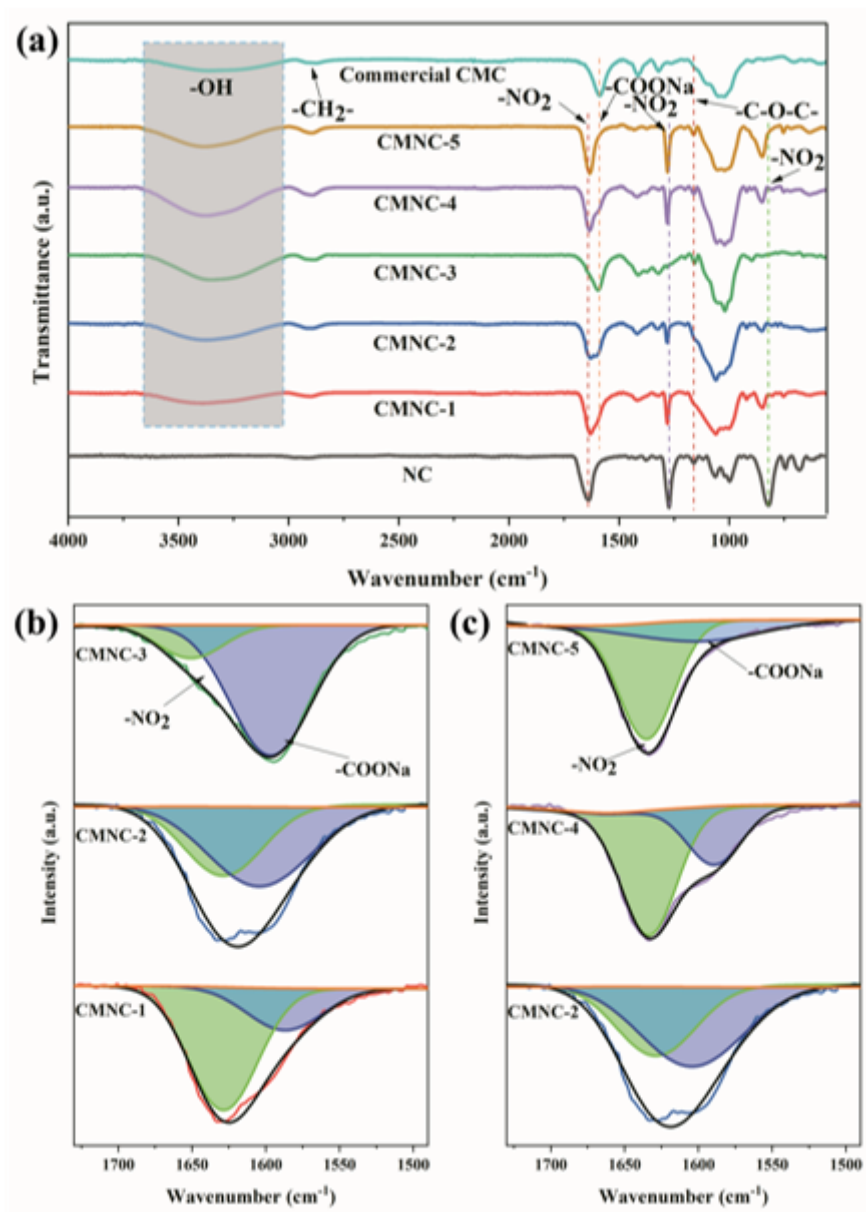


Figure 1



Figure 4

Elemental composition analyses of samples

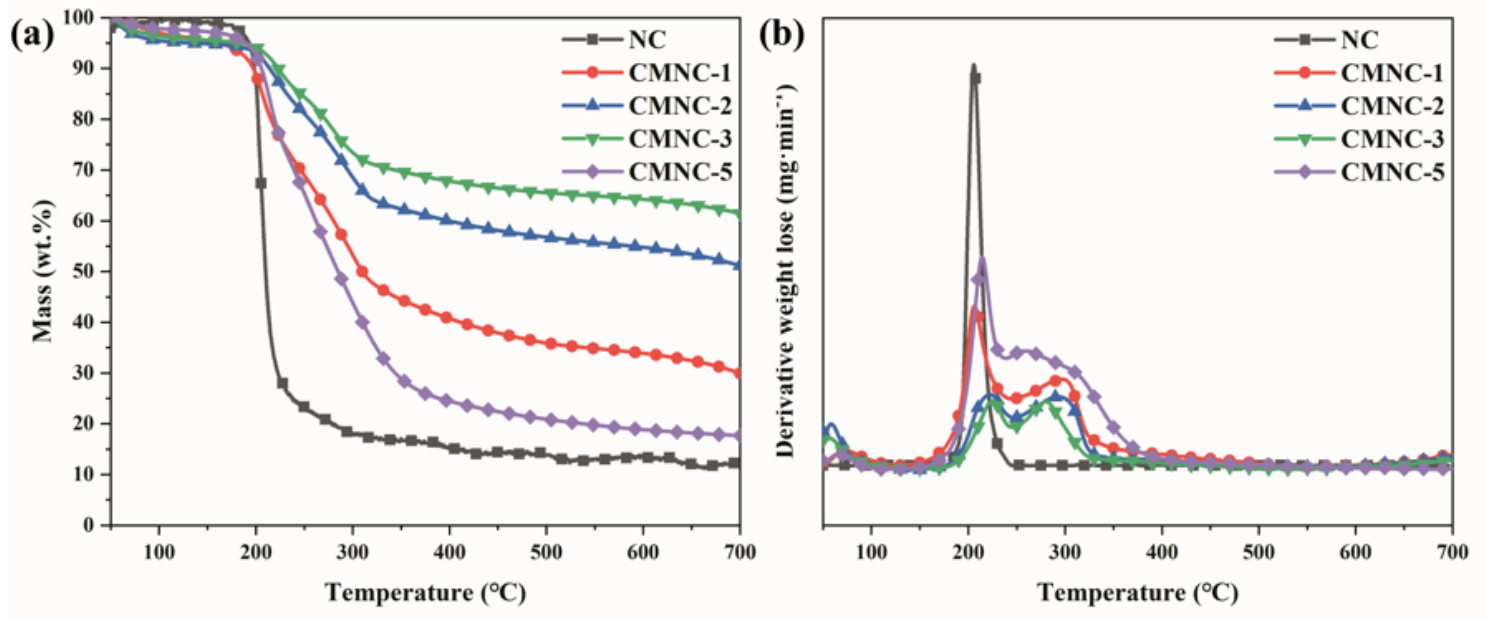


Figure 5

Thermal behavior of Nitrocellulose (NC) and sodium carboxymethyl-nitrocellulose (CMNC) samples with  $\beta=10\text{ }^{\circ}\text{C}\cdot\text{min}^{-1}$ : (a) TG and (b) DTG

Figure 6

IR spectra at  $T_x$ ,  $T_{in}$ ,  $T_1$ ,  $T_f$  during the degradation of NC (a) and CMNC-2 (b).

## Supplementary Files

This is a list of supplementary files associated with this preprint. Click to download.

- [Scheme1.png](#)